

The flow field in a high aspect ratio cooling duct with and without one heated wall

Henrik Rochlitz¹ · Peter Scholz¹ · Thomas Fuchs²

Received: 27 May 2015 / Revised: 28 August 2015 / Accepted: 6 October 2015 / Published online: 11 November 2015
© Springer-Verlag Berlin Heidelberg 2015

Abstract The flow in a high aspect ratio generic cooling duct is described for different Reynolds numbers and for adiabatic as well as non-adiabatic conditions. The Reynolds number is varied in a range from 39,000 to 111,000. The generic cooling duct facility allows for applying a constant temperature on the duct's lower wall, and it ensures having well-defined boundary conditions. The high-quality, optical noninvasive measurement methods, namely Particle Image Velocimetry (2C2D-PIV, i.e., two velocity components in a plane), Stereo Particle Image Velocimetry (3C2D-PIV, i.e., three velocity components in a plane) and Volumetric Particle Tracking Velocimetry (3C3D-PTV, i.e., three velocity components in a volume), are used to characterize the flow in detail. Pressure transducers are installed for measuring the pressure losses. The repeatability and the validity of the data are discussed in detail. For that purpose, modifications in the test facility and in the experimental setup as well as comparisons between the different measurement methods are given. A focus lies on the average velocity distribution and on the turbulent statistics. The longitudinal velocity profile is analyzed in detail for Reynolds number variations. Secondary flows are identified with velocities of two

orders of magnitude smaller than the longitudinal velocity. Reynolds stress distributions are given for several different cases. The Reynolds number dependency of $\overline{u'^2}$ and $\overline{v'^2}$ is shown, and a comparison between the adiabatic and the heated case is given. $\overline{u'^2}$ changes significantly when the lower wall heat flux is applied, whereas $\overline{v'^2}$ and $\overline{u'v'}$ almost stay constant.

1 Introduction

Turbulent flows in ducts with rectangular cross sections and high aspect ratios are prevalent in many technical applications. Many of these duct flows serve as cooling channels for surrounding surfaces or devices. Typical engineering examples of such flows range from cooling channels in hybrid electric vehicle motors to the cooling system in regeneratively cooled rocket engines. A detailed understanding of these flows is important for the cooling channel's optimal design and for lifetime predictions of the cooled devices.

The flow in high aspect ratio cooling ducts is highly affected by secondary flow structures perpendicular to the bulk flow direction, which appear in the duct's corners. The velocity magnitude of the secondary flows is typically some orders of magnitude smaller than the bulk flow velocity. Nevertheless, the effect of the secondary flows on the bulk flow and on heat and momentum transport has to be considered when designing or simulating these types of flows. Despite the importance of duct flows with rectangular cross sections, only few contributions publish detailed experimental results on that topic.

First detailed measurements of secondary flows were taken by Brundrett and Baines (1964), Gessner and Jones (1965) and Launder and Ying (1972). A hot-wire system

✉ Henrik Rochlitz
H.Rochlitz@tu-braunschweig.de

Peter Scholz
P.Scholz@tu-braunschweig.de

Thomas Fuchs
Thomas.Fuchs@unibw.de

¹ Institut für Strömungsmechanik, Technische Universität Braunschweig, Hermann-Blenk-Str. 37, 38108 Braunschweig, Germany

² Institut für Strömungsmechanik und Aerodynamik, Universität der Bundeswehr München, Werner-Heisenberg-Weg 39, 85577 Neubiberg, Germany

was used in all these experiments to measure the velocities in the air flow. The ducts were of quadratic type. The secondary flows are described thoroughly in these publications.

A noninvasive measurement technique was applied by Melling and Whitelaw (1976) to quantify the flow in an adiabatic, rectangular duct with an aspect ratio of 1. They used a laser Doppler anemometer system to measure a water flow at a Reynolds number of 42,000. The mean velocity profile in longitudinal direction at the center line shows a non-uniform profile at around 80 % of the duct's height. Secondary flows were measured with a velocity in the order of 1 % of the longitudinal velocity, but might have large uncertainties due to the measurement setup. Nowadays, in typical applications the aspect ratio is much larger and the Reynolds number much higher.

The influence of heated walls was analyzed by Wardana et al. (1992, 1994). They also used a laser Doppler anemometer system to measure the velocity in discrete points in an air flow at a rather low Reynolds number of 14,000. They described the change in the flow with wall heating in comparison with an adiabatic flow. It is mentioned that the wall heating affects the rms velocity fluctuations, but that this effect is temperature dependent.

A mean velocity profile in the symmetry plane of an adiabatic rectangular duct with an aspect ratio of 11.7 is given by Monty (2005). The velocity profiles were obtained by measuring the pressure with a pitot-static probe. The mean velocity profiles show a characteristic behavior influenced by secondary flows. However, only a single profile in the symmetry plane is provided for an adiabatic duct such that this case cannot really serve as a validation case for numerical simulations.

A high-quality, spatially resolving and noninvasive measurement technique like PIV was not used in any of the described experiments. All data were acquired at discrete points.

PIV results of turbulent channel flows are available, for example by Kwon et al. (2014). However, in this case the channel width was one order of magnitude larger than the channel height and the measurement position was at the center of its width. Thus, secondary flows do not have a relevant influence on the flow at the measurement location.

In contrast, several flow ducts with rectangular cross section have been studied by numerical investigations in the last decade. Cooling duct flows with aspect ratios of 1–7 were studied by Vinuesa et al. (2014) by means of a direct numerical simulation. Different secondary flow structures, e.g., vortex pairs and triplets in the corners, are clearly visible. Also, streamwise velocities are given. They mentioned that the array of secondary vortices in the duct significantly impacts the flow physics at the core.

Vázquez and Métais (2002) described large eddy simulations of a flow through a square duct. They considered

an isothermal duct and a duct with a high temperature prescribed at one wall. They observed an increase in size and intensity in the secondary flows located near the heated wall in comparison with the isothermal case. Moreover, a decrease in turbulence intensity near the heated wall due to the enhanced viscosity effects in these regions is reported.

The influence of streamwise vortices on turbulent heat transfer in rectangular ducts with various aspect ratios is presented by Choi and Park (2013). Contours of the mean turbulent intensities of all three dimensions are given for a case with an aspect ratio of one. The turbulent intensity of the longitudinal velocity component in the center of the duct is about two times larger than the turbulent intensity of the lateral velocity components.

To summarize, in the majority of the experimental and numerical examinations a quadratic duct (i.e., low aspect ratio) was studied. Furthermore, most cases feature relatively small Reynolds numbers. However, ducts with larger aspect ratios at rather high Reynolds numbers are common in most technical applications. Due to the lack of high-quality experimental data of cooling duct flows at high aspect ratios, a generic cooling duct was designed. The optical measurement techniques, namely Particle Image Velocimetry (2C2D-PIV, i.e., two velocity components in a plane), Stereo Particle Image Velocimetry (3C2D-PIV, i.e., three velocity components in a plane) and Volumetric Particle Tracking Velocimetry (3D3C-PTV, i.e., three velocity components in a volume), were used to provide detailed information about the mean velocity fields and local fluctuations at different positions in the duct. First, in Sect. 2.1, some remarks about the generic cooling duct and the supporting facilities will be given. The experimental setup(s) and analysis methods for PIV and PTV will be described in Sect. 2.3. The results, including a detailed study of the flow quality, will be discussed in Sect. 3. One major intention is to provide a dataset for the validation of numerical studies. Therefore, the Reynolds number and heat flux were chosen to be of an order of magnitude, which allows for large eddy simulations (LESs) of this case. At the same time, the case was kept simple with a rectangular duct and only one heated wall.

2 Experimental setup

2.1 Generic cooling duct facility

The measurements were taken in a generic cooling duct with water as the working fluid (Rochlitz and Scholz 2014). The duct has a rectangular cross section with an average width of $w = 6.23$ mm and a height of $h = 26.10$ mm. Consequently, the duct has an aspect ratio of 4.2 and a hydraulic diameter of $d_h = 10.06$ mm. The length is $l = 600$ mm,

i.e., 60 times the hydraulic diameter, which ensures a developed turbulent flow in the duct as well as a developed thermal boundary layer on the lower wall. The two side walls and the top wall are made from 10-mm polymethyl methacrylate (PMMA) sheets to provide optical access to the duct flow.

The lower wall (material: copper, Cu-HCP) can be heated and forms the tip of a so-called heat nozzle (Fig. 1). This ensures a uniform temperature distribution at the lower wall. The heat nozzle is a massive block of copper with a tapered tip. Twenty-three cartridge heaters with an overall electric power of 14 kW are embedded in the heat nozzle's lower part. The temperature of the copper block is measured along the tip, very close to the duct, by means of 23 resistance thermometers along its length. These thermometers and the heaters are connected to a closed-loop control system to control the temperature at the tip. This heating system was validated by means of an infrared thermography system. The mean deviation from the temperature set point was 0.04 K, and the maximum deviation was 0.27 K. Hence, using the control and taking advantage of the heat nozzle, the temperature at the duct's lower wall can be assumed to be constant over time and space and is independent from the effective heat flux into the flow. In the following, T_w denotes the wall temperature, which is regulated by the heat nozzle. Heating is applied only at the lower wall and only in the test section (red area in Fig. 2).

The roughness average of all walls (PMMA and copper) is $R_a < 0.1 \mu\text{m}$. Hence, all walls are hydraulically smooth. The copper surface was treated such that it has the same roughness as the PMMA.

The system is a closed cycle. The water flows from a tank through an electromagnetic flowmeter Promag 10P40 by Endress+Hauser, which is the primary device to determine the flow rate and, thus, bulk velocity. Electromagnetic flowmetering is, by its principle, independent of the density.

The pump is a 4.2 kW centrifugal pump. An industrial rated flow straightener is mounted behind the pump to break possible vorticity induced by the pump. Smooth transitions are installed at the inlet and outlet of the duct geometry to adapt them to the geometry of the piping. A feed line with the same width, height and length as the

duct test section ensures a fully established turbulent flow already at the beginning of the test section. A flow straightener is mounted just upstream of the feed line to ensure a homogeneous inflow. This flow straightener was removed for one test point to test whether the flow is sensible to any disturbance that might come from the pump or the inflow. The connection from the pump to the feed line is curved due to practical reasons. To analyze the influence of this curvature, 2 m of additional straight tubing has been installed upstream of the second flow straightener in one test. The feed line itself—in contrast to the test section—is not heated; the lower wall is build of aluminum, and the two side walls and the top wall are build of 10-mm PMMA sheets.

The water flows back to the tank when leaving the heatable duct test section. The water in the tank can be heated using immersion heaters with an installed total heat output capacity of 9 kW or cooled via a cooling system with a maximum rated cooling power of 25 kW. Both systems together ensure constant and steady bulk flow temperature T_b and, thus, continuous operation, regardless of whether the flow in the duct is adiabatic or not.

Two absolute pressure transmitters of the type Wika A-10 (range 0–6 bar, effective precision: 0.1 %) are mounted between the feed line and the duct and at the downstream end of the duct to measure the pressure loss across the test sections. 4-wire PT-100 class AA resistance temperature detectors (RTDs) are mounted at the same positions to measure the fluid bulk temperature. The reference fluid bulk temperature T_b is measured upstream of the test section.

By measuring all these values and controlling the secondary equipment (coolers, heaters, pump, etc.), the boundary conditions of the generic cooling duct setup are well known. The bulk temperature can be adjusted with an accuracy of ± 0.2 K. Bulk temperatures in the range 20–60 °C and wall temperatures in the range 20–100 °C are possible. For the experiments described here, the flow rate was varied in the range between $\dot{V} = 38$ –62 l/min.

Figure 2 provides a sketch of the relevant duct section; bulk flow is from left to right. The left part is the feed line, the right part is the test section duct, which can be heated at the lower wall (indicated in red color). The

Fig. 1 Overview of the generic cooling duct setup

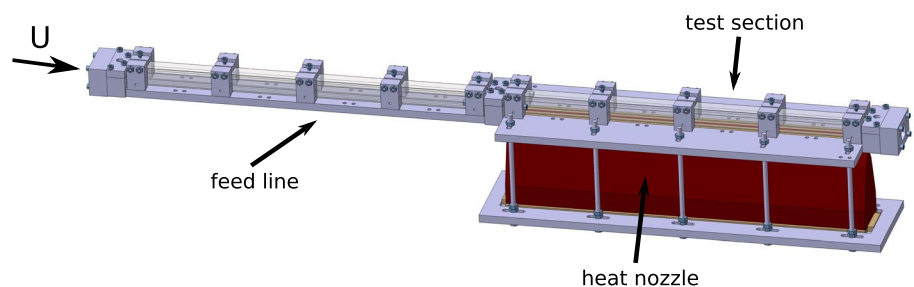
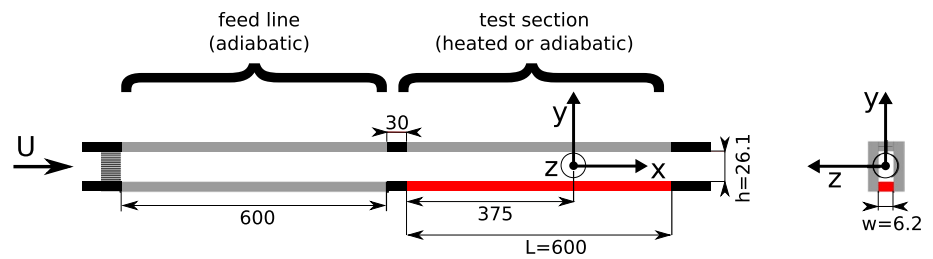


Fig. 2 Sketch of the generic cooling duct with dimensions and coordinate system, all dimensions are in mm. The wall is heated in the red area



coordinate system axes are indicated, with x pointing in streamwise direction, y is along the height and z is along the width, respectively. This system will be used throughout this contribution; the origin lies in the center of the test section.

All velocity data are normalized by the bulk flow velocity,

$$u_b \equiv \frac{\dot{V}}{A}, \quad (1)$$

where A is the cross-sectional area of the duct and \dot{V} is the flow rate. The mean flow rate is measured with an uncertainty of $<0.5\%$. However, due to the turbulence in the piping, the value fluctuated during a test run by approximately 0.6% . To account for this, the flow rate was logged during each test run while acquiring the images for the PIV/PTV. In the post-processing, the average flow rate of each individual run was used to normalize the data with Eq. 1. Intentionally, the pump was driven at constant rpm and *not* closed-loop controlled with the flow rate, to prevent any instationarity that would otherwise come from the controller input to the pump.

2.2 Flow cases

Mainly three cases will be discussed herein, the parameters of which are given in Table 1. The nominal flow rate is always constant at 50 l/min. The Reynolds number is calculated with the bulk flow velocity u_b , the physical properties at the corresponding bulk temperature T_b (namely ν) and the hydraulic diameter of the duct as the characteristic length. Case 1 in comparison with case 2 basically is a Re variation by means of an increased bulk temperature T_b . To achieve a nominally adiabatic case, the lower wall is also heated for case 2, to maintain $T_w = T_b$. Case 2 and case 3 provide a direct comparison between a nominally adiabatic case with a heated lower wall at the same Re . The Grashof number, Gr , at case 3 is approximately 800,000. The ratio Gr/Re^2 is 6.6×10^{-5} which means that all natural convection motions can be neglected since the ratio is far below 1 (Bergman et al. 2011). Forced convection is dominating the heat transfer. For all cases and in all analyses, the properties of the water (i.e., density ρ and viscosity ν) are based on standard values and were not measured directly.

Table 1 Characteristic parameters for the configuration of the generic cooling channel experiment

Case	\dot{V} (l/min)	T_b (°C)	T_w (°C)	\dot{q} (MW/m ²)	Re (-)
1	50	20	20	0	52,000
2	50	60	60	0	111,000
3	50	60	100	1.1	111,000

Beside the base cases discussed above, two different sweeps of Re were performed, to verify the comparability of case 1 and case 2. This was done by two means, (1) by increasing the flow rate \dot{V} at constant bulk and wall temperature, and (2) by stepwise increasing T_b from 20° to 60° , thus decreasing the viscosity at a constant flow rate. For the latter, of course $T_w = T_b$ was maintained. However, the side walls and the top wall are made from PMMA sheets to provide optical access to the cooling duct. Thus, the outward surfaces of the walls are exposed to the ambient air temperature, which is at approximately 20°C . Hence, if the bulk temperature is larger than the ambient temperature, there can be a small heat flux across the sides and top wall. However, a typical test is very “slow”, i.e., in any case the heat flux over the PMMA would be stationary.

2.3 Optical setup and analysis methods

The 2C2D-PIV, 3C2D-PIV and 3C3D-PTV techniques were used to measure the flow field in the generic cooling channel duct. The results from the 2C2D-PIV and 3C2D-PIV measurements provide detailed information about mean velocities and fluctuations for two, respectively, three, velocity components in the considered plane. Complementary to PIV, 3C3D-PTV is used to provide volumetric information of the mean velocity components. PIV and Stereo-PIV were applied in the center section and Volumetric PTV in the entire volume of the duct.

2.3.1 PIV

The optical setup including the laser, the light sheet optics and the cameras is presented in Fig. 3. The length of the field of view (FOV) is typically around 50 mm, and the

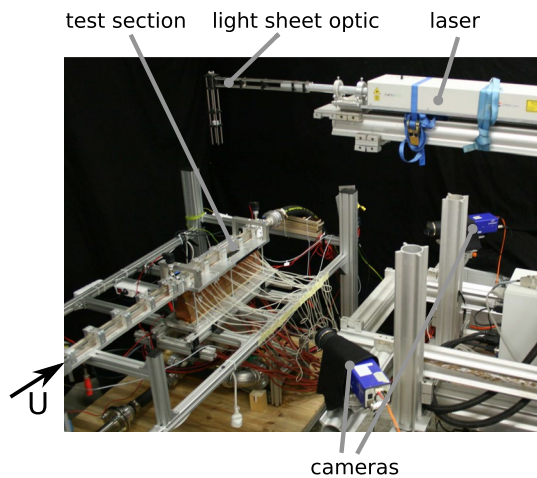


Fig. 3 Experimental setup

height is the duct's height. Silver-coated hollow glass spheres with a diameter of $10\ \mu\text{m}$ were used as tracer particles, illuminated by a Litron Nano-T PIV double-pulse Nd-YAG solid-state laser, which is mounted above the duct. The laser has a wavelength of 532 nm, and typically an energy of around 100 mJ per pulse was used. The laser light sheet was focused by a plano-concave lens with a focal length of $-50\ \text{mm}$ and a plano-convex lens with a focal length of 100 mm. After passing the focusing optics, the laser beam was adjusted to be orthogonal to the corresponding axis by means of a mirror. The beam then passed through a cylindrical lens with a focal length of $-25\ \text{mm}$ to form the light sheet. The laser optical setup was mounted to the laser head and adjusted and arranged by means of the Linos microbench system.

One, respectively, two, PCO SensiCam cameras were used for all measurements. The Scheimpflug criterion was met for all setups. The commercial software Davis 7.2.2 from LaVision was employed for all data acquisition and most steps of data analysis.

The laser light sheet thickness was set to 1 mm for 2C2D-PIV and 3C2D-PIV measurements. To measure light sheet thickness, a high-quality vernier caliper was used: The distance between the jaws was increased in 0.1 mm steps and held into the laser light sheet repeatedly until the laser light illuminated the jaws no more. This process ensures a repeatable light sheet thickness when re-adjusting the laser. However, note that this is not necessarily the effective thickness, since the light sheet features some Gaussian intensity distribution and it cannot be determined, which incident light intensity is necessary to illuminate a tracer particle which then is detected by the cameras. Also, the adjustment is done at low laser power, but the measurements at higher power. Therefore, the effective light sheet thickness might be different.

A spatial calibration was performed for all measurements. This calibration process was performed as follows: A small cap in the test section's top wall is removed to gain physical access to the test section. Then, the test section is filled with water to match the refractive index of the subsequent measurement. After that, the calibration plate is inserted and adjusted in the test section. The calibration plate is mounted at a high-precision traverse to allow for shifts in z direction. Of course, both the calibration plate and the traverse are adjusted identical. This adjustment process was done very carefully for a best possible calibration. The calibration plate was traversed in z direction, and images were taken at the center of the light sheet for 2C2D-PIV, 0.5 mm before and behind the center of the light sheet for 3C2D-PIV and over the entire duct width with an increment of 0.5 mm for 3C3D-PTV. The calibration grid's width in x direction is 30 mm, and its height in y direction starts at 0.5 mm above the lower wall and ends over the duct's top wall. The FOV includes approximately 50 mm in x direction and the complete duct height.

In fact, the calibration process is complex and due to the relatively small size of the duct (and the plate, respectively); especially, the angularity relative to the physical x , y , and z coordinates is subject to inaccuracies (typically of the order of 0.5°), which will be discussed in Sect. 3.1.

In the case of a heated wall, the particle images have been checked, whether any blurring or aberration exists due to density gradients and, thus, refraction. However, this is not the case.

A self-calibration was applied for 3C2D-PIV measurement results (Wieneke 2005). The self-calibration shifts the two-dimensional plane in that way that it is adjusted exactly in the middle of the laser light sheet. This self-calibration eliminates errors in the vector calculation process due to misalignment of the calibration plate with respect to the light sheet position. However, the error in angularity of the calibration plate with respect to the duct's coordinate system is not corrected.

One thousand and five hundred double-frame images were processed for PIV data analysis for each measurement. A multipass technique with decreasing windows size from $64\ \text{px} \times 64\ \text{px}$ to $16\ \text{px} \times 16\ \text{px}$ with window shifting and 50 % overlap with three passes in total was applied. The spatial resolution (distance between neighboring vectors) is 0.26 mm for 2C2D-PIV and for 3C2D-PIV. The uncertainty in velocity normalized by the bulk velocity u_b is approximately 2×10^{-4} for the 2C2D-PIV and 3C3D-PIV systems for all velocity components. The statistical convergence for 2C2D-PIV and 3C2C-PIV is plotted in Fig. 4 for $\overline{u^2}/u_b^2$ with data from one vector in the center of the duct. The number of double-frame images used for calculating $\overline{u^2}/u_b^2$ is plotted versus the variance between individual ensembles of u^2/u_b^2 . The data for 3C3D-PTV

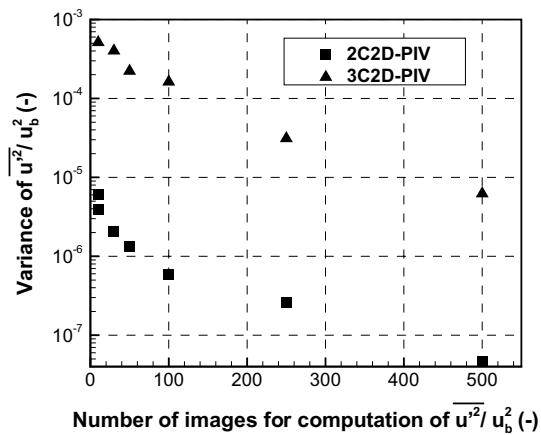


Fig. 4 Statistical convergence of $\overline{u^2}/u_b^2$ for one vector at $y \cdot 2/h = 0$

are not shown here because these data are not used in our paper. The variance, even with rather small ensemble size, is $<1\%$ of $\overline{u^2}/u_b^2$ (as will be shown later). Thus, the turbulent data can be assumed to be converged with respect to the number of images.

2.3.2 3C3D-PTV

Three-dimensional Particle Tracking Velocimetry yields a volumetric, three-component (3D3C) velocity field (Maas et al. 1993). The setup of the equipment was basically the same as for the 3C2D-PIV measurements, with the exception that the laser light sheet was modified to illuminate the entire width of the test section duct. Furthermore, the seeding concentration was rather low to avoid ambiguities in matching corresponding particle images on the two sensors (Fuchs et al. 2014). The two cameras acquired double-frame images of the volume from two different perspectives with an angle of 90° between the cameras.

The imaging system is calibrated using point correspondences, comprising image coordinates on both camera sensors and the physical coordinates of these points. With these point correspondences, the fundamental matrix F , as well as the camera matrices P_1 and P_2 of each camera, is computed.

After acquisition, an average image of all recordings is subtracted from each single image to eliminate background reflections, followed by a sliding minimum subtraction over a range of 3×3 pixels, and an intensity normalization using local averages. For the particle image detection, the preprocessed recordings are binarized to separate the particle images from the background. A 2D Gaussian fit is applied to the detected particle images using the background subtracted images to determine the image coordinates of their center with subpixel accuracy. Corresponding particle images on the two camera sensors are matched

using epipolar geometry. The spatial particle locations are triangulated from the matching particle image center locations on the two sensors. A nearest-neighbor tracking algorithm is employed to derive the velocity information from the double-frame data.

Two thousand and five hundred images were processed for the 3C3D-PTV analysis. After processing, the vectors are sorted into bins to enable a statistical analysis, where the bins are of the size of 0.5 mm in y and z directions, with one single bin in x direction (i.e., the average over the x range is taken). The vector density of PTV is equivalent to the distance between middle of neighboring bins and is 0.5 mm. The average number of particles in each bin is 400. It should be noted that, due to the low particle density required, only the mean values of the flow are significant, while the turbulent statistics are not converged. Therefore, 2C2D-PIV and 3C2D-PIV have been used complementary to the 3C3D-PTV technique. Normalized with u_b , the maximum uncertainty in velocity is approximately 1.8×10^{-3} for the 3C3D-PTV technique.

3 Results

3.1 Consistency, repeatability, accuracy of the data

The first section is dedicated to a comparison with some variations in the setup and between different measurement techniques, to validate consistency and repeatability. Case 1 from Table 1 was set for all of these tests. The flow itself will be discussed later; therefore, we focus on the profile of longitudinal velocity, or turbulence, respectively, in the center section of the duct $z \cdot 2/w = 0$.

The duct flow is driven by a centrifugal pump, and the infrastructure is connected to the duct with standard piping. To ensure that neither the pump, nor the piping or the transitions have any influence on the flow, tests were run with and without a flow straightener upstream of the feed line, as well as with an additional feed line element. Furthermore, to ensure that the flow in the center of the test section is fully developed, measurements were taken at three different positions x/l along the section. Figures 5 and 6 summarize the results. The differences between the individual datasets are negligible, since only the test without the flow straightener shows some small asymmetry. Therefore, it seems certain that the flow in the duct is a fully developed, self-similar turbulent duct flow. The straightener was used for all subsequent test runs, while the additional feed line was not used, since it makes the test stand more unwieldy, without actually increasing the flow quality.

As outlined in the proceeding, three measurement methods have been used complementary: 2C2D-PIV, 3C2D-PIV as well as 3C3D-PTV. Each of these techniques has its specific advantages (and disadvantages), most important

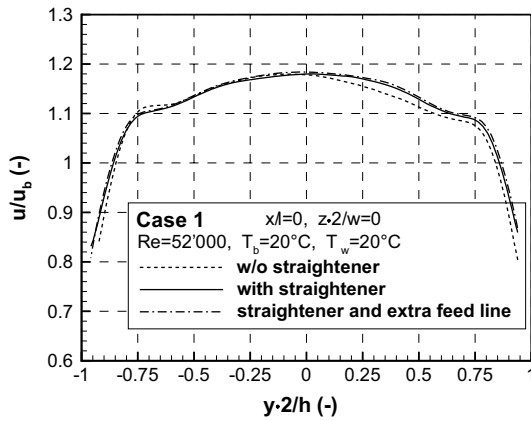


Fig. 5 Velocity profiles in the center section with different inflow sections

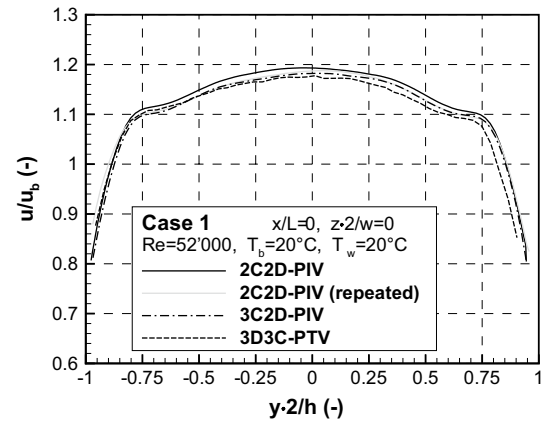


Fig. 7 Velocity profiles in the center section acquired with different measurement techniques, namely 2C2D-PIV, 3C2D-PIV and 3C3D-PTV

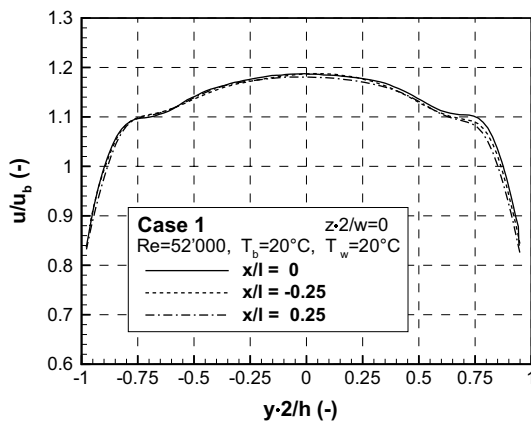


Fig. 6 Velocity profiles in the center section at different positions along the test section

here, 3C3D-PTV allows a full volumetric view on the flow. However, due to inherently low particle density, the turbulent statistics are not converged, the secondary motions are noisy and the spatial resolution is not too high.

To check for consistency and repeatability, the data acquired with the different techniques are compared in Fig. 7. The profiles feature some deviations in velocity as well as some spatial mismatch. The velocities vary by $\sigma_{u/u_b} \approx 0.018$ or 1.5 % of the peak velocity, respectively. The spatial mismatch can be up to 2 % of the duct height. We think that both velocity and spatial mismatch originate from limited repeatability in the spatial calibrations, especially for 3C2D-PIV and 3C3D-PTV. Due to the small dimensions of the duct, the thick PMMA sidewalls necessary to stand the inner pressure and a complicated calibration process, where the duct needs to be filled with water, while physical access to traverse the calibration plate must be granted, the calibration process has some uncertainties in positioning the plate. In conclusion, the repeatability of

the test stand is around 1–2 % in both velocity and position. However, note that the uncertainty of velocity and position in *one* test (i.e., when not comparing data over different calibrations) is more than one order of magnitude better than test-to-test repeatability. Therefore, the conclusions that will be drawn in the subsequent sections will mostly be based on comparisons within *one* test, notwithstanding that the absolute values feature the uncertainty of repeatability.

Finally, when it comes to turbulence values, stochastic measurement noise might overlay the fluctuations and increase the statistical averages. This is typically more of a problem for 3C2D-PIV, as compared to standard 2C2D-PIV, because the oblique viewing angles through the thick PMMA walls decrease particle image quality and, thus, SNR. In order to validate the Reynolds stresses from the 3C2D-PIV datasets, they are compared to the 2C2D-PIV data in Fig. 8. The two datasets coincide quite well. Some differences occur in longitudinal stress $\overline{u'}$, where the 3C2D-PIV data show a slight asymmetry to the duct centerline. Likely, this is due to minor differences in the positioning and orientation of the laser light sheet, since both tests were done with a physically different setup. Hence, these differences are related to a limited repeatability of the spatial positioning, the accuracy of which was discussed in Sect. 2.3. Based on this comparison, the repeatability of the level of Reynolds stresses can be quantified to be around 10 %.

Finally, uncertainties in the results occur, if the calibration plate is not aligned with the physically effective x -, y - and z -coordinate directions, which can happen due to a complicated calibration process (as described above). Since, in a fully symmetric duct flow, $\overline{v}/u_b \equiv 0$ and $\overline{w}/u_b \equiv 0$, these values have been used to quantify possible inaccuracy of the coordinate directions. Based thereon, the

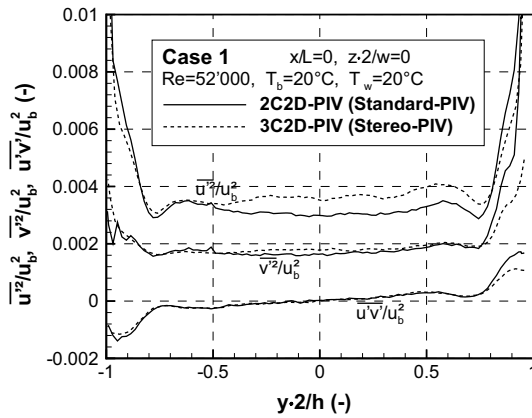


Fig. 8 Profiles of turbulent stresses in the center section measured with 2C2D-PIV and with 3C2D-PIV

accuracy of the axis direction for the 3C2D-PIV results is assumed to be of the order $\sigma_\zeta \approx 0.5^\circ$.

3.2 Mean flow and case comparison

Figure 9 summarizes the integral pressure losses with the pressure loss coefficient λ , which is calculated as

$$\lambda \equiv \left| \frac{\Delta p}{l} \right| \cdot \frac{d_h}{\rho u_b^2}, \tag{2}$$

where Δp is the pressure difference measured with the two sensors upstream and downstream of the test section duct, and ρ is the density based on standard properties of water, including the effect of temperature.

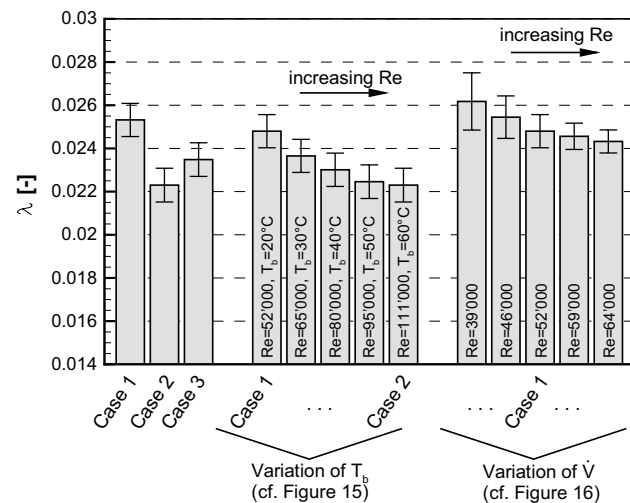


Fig. 9 Pressure loss coefficient λ for all cases studied herein; refer to Table 1 for case descriptions

On the left-hand side of Fig. 9, the three cases are compared directly. The right part shows the pressure loss coefficients for the Re variations described in Sect. 2.2. As generally expected, the pressure loss coefficient decreases with increasing Re . It is worthwhile to note that applying a heat flux at the lower wall (case 3) actually increases the integral pressure loss, if compared to the same Re , but without heat flux (case 2).

To discuss the associated flow structure, the 3C3D-PTV data are used first. The normalized, longitudinal velocity component u/u_b is depicted in Fig. 10 for the three cases defined in Table 1.

In fact, the secondary structures are not very clearly visible in the 3C3D-PTV data. Since the frame separation Δt must be set based on the bulk velocity u , and the secondary flow is two orders of magnitude smaller, together with inherently low particle density, a vast number of images would have been necessary for smooth results of v and w . However, by comparing the 3C2D results and the data from the 3C3D-PTV a conceptual sketch can be drawn of the secondary structures in the duct, which is shown in Fig. 11. As generally expected, a pair of counter-rotating vortices exists, which is located in the region $y \cdot 2/h \approx \pm 0.7 \dots 0.8$ and $z \cdot 2/w \approx \pm 0.6 \dots 0.8$. The data of the flow in the duct seem slightly asymmetric, probably due to slight misalignment of the laser sheet (already less than the aforementioned 0.5° would explain the asymmetry). However, the influence of the vortex pair can also be seen very clearly in the v -component from the PIV result for $z \cdot 2/w = 0$ shown in Fig. 13, where a local maximum (or minimum) of v occurs at $y \cdot 2/h = \pm 0.70 \dots 0.75$. The PIV results also show that the v -component will change sign in between

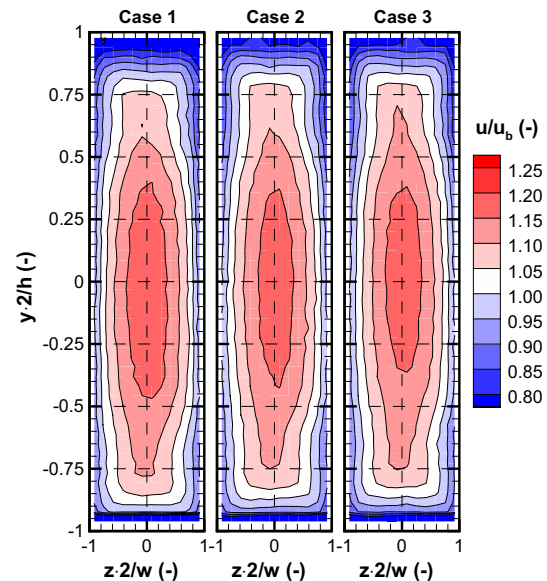


Fig. 10 Case comparison of mean longitudinal velocity, 3C3D-PTV

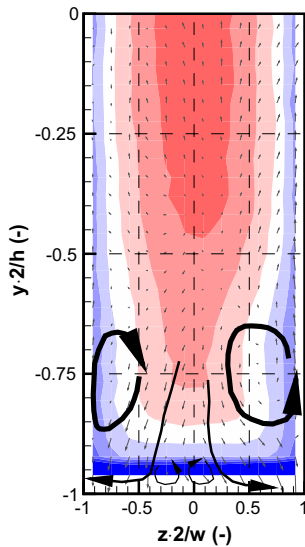


Fig. 11 Illustration of secondary structures; vectors only for visualization

these vortices and the wall. This is clearly due to a pair of smaller vortices at $y \cdot 2/h = \pm 0.90 \dots 0.95$. The larger vortices are also the reason for the shape of the profile of longitudinal velocity, with the characteristic inflection point just at the position of the vortices.

The three cases feature rather small changes in the average flowfield, although Re doubles from case 1 to case 2 and a significant heat flux is applied in case 3. It can be seen in the v -profile in Fig. 13 that heating the lower wall slightly strengthens the vortices (peak amplitude of v becomes larger, particularly for the vortex pair closer to the wall) and lifts them a little away from the heated wall. But in summary, the mean flow is not very prone to the changes introduced by the three cases. Though the data are more noisy, the same conclusions hold from the 3C3D-PTV data (not explicitly shown here). The structure of the secondary flows agrees with already published studies about duct flows with similar aspect ratios but much lower Reynolds numbers, for example (Vinuesa et al. 2014). The maximum secondary flow velocities are in the order of 1 % of u_b which is in the same order of magnitude as for available data on secondary flows, for example (Gessner and Jones 1965; Melling and Whitelaw 1976). However, no identical problem has been investigated so far, and thus, no detailed comparison is possible.

The main difference in the mean velocities is that the bulk longitudinal velocity u_{max} , near the centerline, slightly changes. The data were extracted and are summarized in Fig. 12. Here, the data for the case comparison in the left part of Fig. 13 represent the average and the standard deviation across all datasets, where a direct comparison between the three cases was done [that is, the 3C3D-PTV data (Fig. 10), the 3C2D-data (Fig. 13) and the data of the

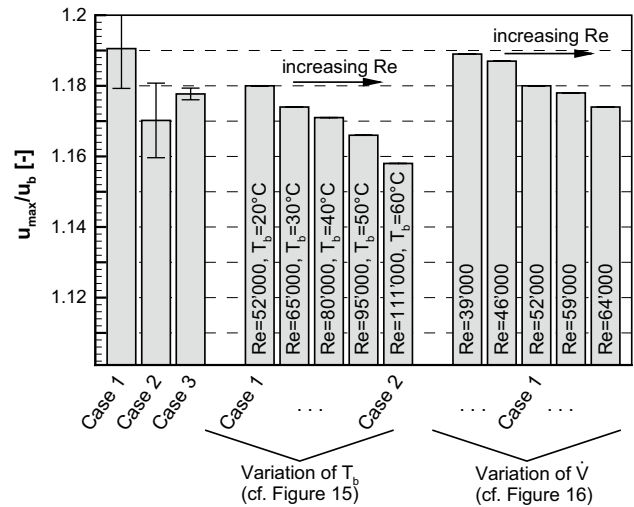


Fig. 12 Peak velocity variation for all cases studied herein; refer to Table 1 for case descriptions

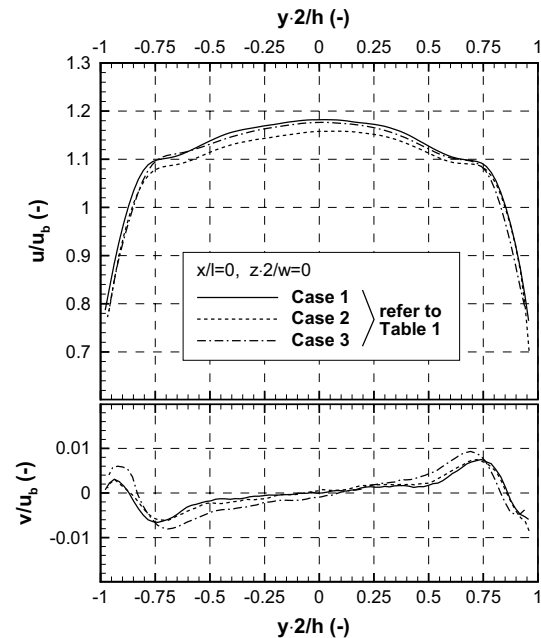


Fig. 13 Case comparison of mean longitudinal and vertical velocity

transversal profiles (Fig. 14)]. In this sense, the errorbars represent the limited repeatability and *not* the individual accuracy of the comparison, but they show that the conclusions hold for all comparisons.

As can be seen from this figure, the core velocity variation can be 2 %, where an increase in Re (from case 1 to case 2) decreases the core velocity, while then applying a heat flux at the lower wall (case 2 to case 3) increases $u_{max.}/u_b$. In order to verify that the comparison between case 1 and case 2 is significant, a stepwise variation of

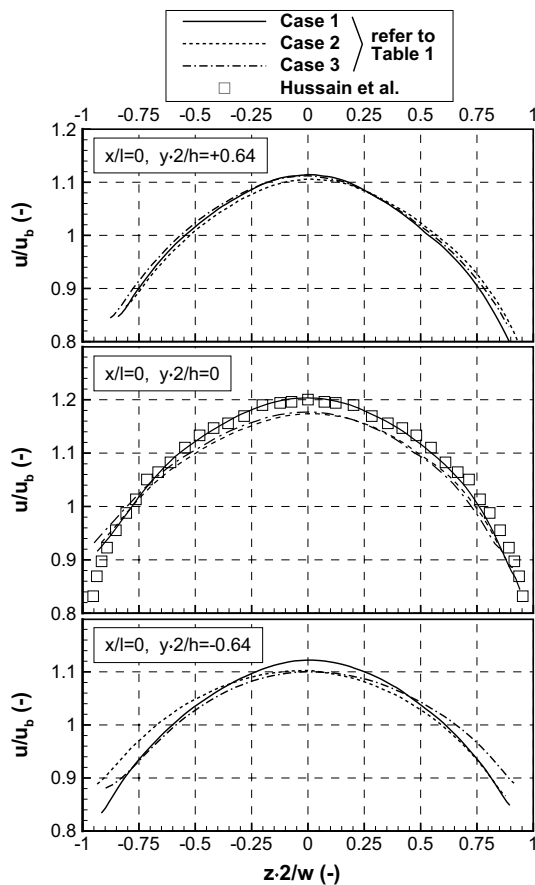


Fig. 14 Profiles of mean longitudinal velocity across the duct width for the three cases and in comparison with data from Hussain and Reynolds (1975)

Reynolds number was also done by two methods, as already mentioned before. As can be seen from this Re variation studies, the results are significant; in general, it seems that $u_{\max.}/u_b$ is proportional to the integral pressure loss shown in Fig. 9.

Finally, we recall that all data for a direct comparison of the cases are generated in *one* setup, basically all test points were run successively without re-calibration or without *any* modification of the optical setup. Therefore, the uncertainty of repeatability, which is discussed in Sect. 3.1, is not a matter to these data. Also, the signal from the flow rate sensor (which is the means to determine u_b) was cross-checked several times, to exclude the possibility that the variation of $u_{\max.}$ is caused by a systematic error of u_b .

However, if $u_{\max.}/u_b$ decreases, since the flow rate is the same for all three cases, regions must exist, where u/u_b increases. To find these regions, 2C2D-PIV was applied in three different slices $y = \text{const}$. Figure 14 shows the profiles of u/u_b across the duct width for these three cases. In all optical measurements, the regions close to the walls are challenging to resolve, due to increasing influence of

reflections and strong velocity gradients. Nevertheless, the figure indicated that the velocity profile is “wider,” featuring regions of higher u/u_b closer to the walls, if Re is increased. This somewhat coincides with the expectation, that increasing Re will more and more lead to a top-hat-shaped velocity profile. Here, the effect is more pronounced in the regions of the secondary vortices. The absolute values from Fig. 14 should not be over-interpreted, since the data from this setup cannot be backed up by a complementary technique; also, it can be noted that the difference from case 2 to case 3 in the center section is slightly different here, as compared to Fig. 13 (which was accounted for in the error bars in Fig. 12). In addition, experimental results by Hussain and Reynolds (1975) are given in Fig. 14 for $y \cdot 2/h = 0$. They conducted experiments on the turbulent flow in a duct with an aspect ratio of 18 at a Reynolds number of 7400 (the Reynolds number is adjusted to the definition used in this paper). The velocity of their measurements at $z \cdot 2/w = 0$ is set 1.2 for this plot. Their profile agrees quite well with ours, indicating that the secondary flows in the edges of the duct have minor influence on the shape in the center of the duct. This means that the flow in the center of the duct is nearly like a two-dimensional channel flow. The decrease in velocity seems to be slightly higher in Hussain’s measurements, resulting in a “narrower” profile compared to our measurements. Because their Reynolds number is lower than it is in our cases, this agrees well with the observation of the flow profile’s shape as mentioned earlier. However, because Hussain’s duct shape and Reynolds number are different to the measurements presented in this paper, this comparison should not be over-interpreted.

3.3 Turbulent statistics

This section discusses the turbulent statistics derived from the PIV measurements. We focus on u' - and v' -components, since these can be validated by cross-comparison between the two different methods 3C2D- and 2C2D-PIV, which is shown in Fig. 8. The two techniques were applied independently, and both yielded similar results.

The correlations $\overline{u'^2}$, $\overline{v'^2}$ and $\overline{u'v'}$ are shown in Fig. 15 along the duct centerline for the three cases. While the shear stress $\overline{u'v'}$ is not affected, neither by the Re variation, nor by the heat flux, the longitudinal point correlation $\overline{u'^2}$, in contrast, decreases with increasing Re , as well as with increasing heat flux. The wall normal component $\overline{v'^2}$ is affected by an increase of Re , but not by applying a heat flux. The averages of the fluctuations are in the order of around 5 % of the bulk velocity. Thus, they are not mainly affected by stochastic noise and well larger than the resolution of PIV (which is typically in the order of 0.2 %).

To check the validity of the Re variation, the sequences of different Re values are shown in the following figures.

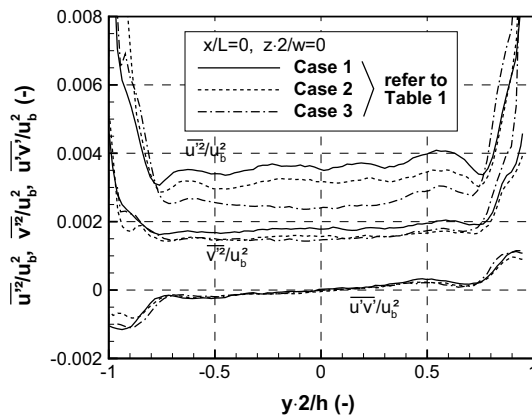


Fig. 15 Reynolds stress distributions for the three different cases

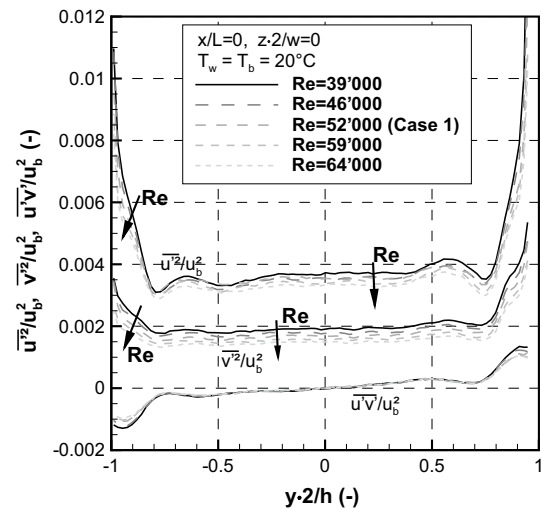


Fig. 17 Reynolds stress distribution for increasing Re by increasing \dot{V} at constant temperatures T_b and T_w

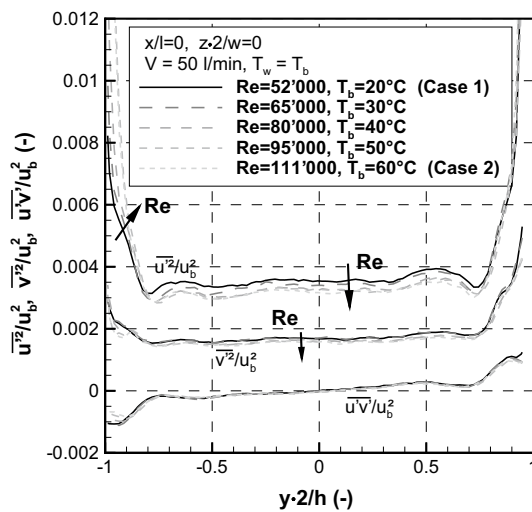


Fig. 16 Reynolds stress distribution for increasing Re by increasing T_b and T_w at constant flow rate

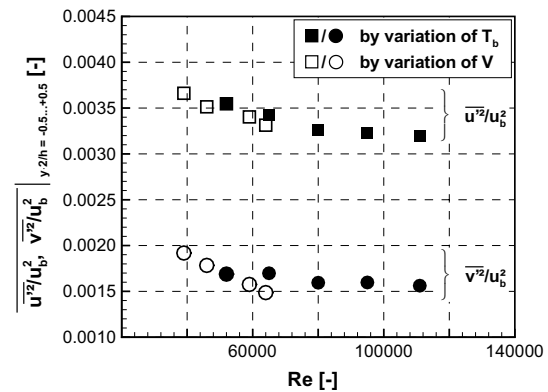


Fig. 18 Influence of Re on the turbulent point correlations in the bulk flow region

Figure 16 shows the variation of Re by increasing the bulk temperature, whereas Fig. 17 is also a Re variation, but with an increased flow rate \dot{V} . In both cases, the shear stress $\overline{u'v'}$ is still unaffected and matches down to line thickness in the bulk flow region.

The point correlations actually show an interesting behavior. As already seen in Fig. 15, both $\overline{u'^2}$ and $\overline{v'^2}$ decrease in the bulk flow region with increasing Re . When comparing Figs. 16 and 17, however, it seems as if the influence on the point correlations is slightly different for the two methods to vary Re . When Re is increased by decreasing the viscosity of the fluid (i.e., increasing T_b), both $\overline{u'^2}$ and $\overline{v'^2}$ decrease also in the regions near the upper and lower wall. In contrast, if Re is increased by increasing bulk flow velocity or flow rate \dot{V} , respectively, $\overline{v'^2}$ is not so much affected near the walls and $\overline{u'^2}$ increases near the walls.

We note that, when increasing Re by varying the viscosity with T_b , the walls of the tunnel are not strictly adiabatic, since they are surrounded by air at ambient temperature and not specifically isolated. Thus, a (negative) heat flux through the PMMA might exist. However, this flux should be rather small, since thermal conductivity of PMMA is small. Furthermore, if we consider the influence of a very significant (positive) heat flux from the heated wall, which is shown in Fig. 15, case 3, $\overline{u'^2}$ decreases in the bulk flow, when a heat flux into the flow exists. So, it is counterintuitive that a negative heat flux through the PMMA (i.e., a cooling effect) should have a similar effect on $\overline{u'^2}$ and $\overline{v'^2}$.

The variation of $\overline{u'^2}$ and $\overline{v'^2}$ in the bulk flow region is furthermore summarized in Fig. 18. An average was taken in the region $y \cdot 2/h = -0.5$ to $+0.5$ and is plotted versus Reynolds number for the two different ways to vary Re . The aforementioned trends for the bulk flow are clearly

visible. It cannot be said from this data, whether the trend, that the gradients for both, $\overline{u'^2}(Re)$ and $\overline{v'^2}(Re)$, decrease in the region $Re \approx 50,000$ is really significant, but it is noted that these variations were done within one single calibration, and the turbulent statistics have been found to be generally quite repeatable. A comprehensive comparison to high-quality LES data is planned to give insight into the turbulent properties for these cases.

4 Summary

A generic cooling duct experiment was described, which allows for the acquisition of high-quality velocity data of a high aspect ratio duct flow, including the effect of heat flux by varying the temperature of one wall. The flow was measured with several different spatially resolving, particle-based optical methods, namely 2C2D-PIV, 3C2D-PIV as well as 3C3D-PTV. The repeatability and validity of the data were discussed in detail. The analysis focused on the average velocity distributions as well as on turbulent statistics. Since the effects of the variations are almost generally small, attention was drawn to case comparisons in one setup (without any recalibration). However, the results are also related to comparisons across different test setups.

The secondary flow structure was found to be rather weak, with mean velocity components v and w being $<1\%$ of the longitudinal flow component. Nevertheless, the characteristic shape of the longitudinal velocity profile is notably influenced by the two vortex pairs in the side ends of the duct. The profile of longitudinal velocity shows deterministic behavior, if the Reynolds number is varied: With increasing Re , the peak velocity in the center of the duct decreases and increases in the regions closer to the walls. These effects are also small, with the peak velocity in the centerline being the most indicative element. At the same time, the pressure loss also decreases with Re , being proportional to the peak velocity in the centerline throughout all cases studied herein.

Beside the mean flow velocities, also the turbulence statistics of the duct flow have been presented for the three cases. In general, when increasing Re , the point correlations of velocity, $\overline{u'^2}$ and $\overline{v'^2}$, decrease in the bulk flow region. The sensitivity to the Reynolds number near the walls was not completely clear, since the trend is of opposite sign, if Re is varied by two different means.

The influence of applying a heat flux from the lower wall is clear as a trend, but cannot be quantified to the full extent, yet, since a stepwise variation was not done. If a heat flux is applied, the peak velocity near the centerline of the duct will increase as compared to the same case at same Re , but with adiabatic walls. Also, the integral pressure loss increases when heating is applied. Regarding the turbulent properties, the point correlation of longitudinal velocity,

$\overline{u'^2}$, in the bulk flow decreases significantly when applying a heat flux, whereas $\overline{v'^2}$ and $\overline{u'v'}$ remain almost constant.

In future work, the influence of heating will be studied more in detail, to be able to describe the variations between case 2 and case 3 with better confidence. Yet, to study a new parameter, the whole set of *all* experiments must be repeated, to assure the quality of the data in view of the limited repeatability. The local temperature of the flow will be measured by means of calorimetric 2-color LIF, to acquire datasets consisting of velocity–temperature correlations. The test stand is able to run at significantly higher mass flow rates; therefore, it seems interesting to acquire data for even higher Reynolds numbers.

Acknowledgments The work has received funding by the German Research Foundation (Deutsche Forschungsgemeinschaft, DFG) within the framework “Sonderforschungsbereich Transregio 40, SFB-TRR40” (Technological foundations for the design of thermally and mechanically highly loaded components of future space transportation systems). The authors acknowledge helpful discussions with the people from Institute of Aerodynamics and Fluid Mechanics, Technische Universität München, who conduct LES simulations of these cases, namely Vito Pasquariello, Thomas Kaller and Stefan Hinkel.

References

- Bergman TL, Lavine AS, Incropera FP, De Witt DP (2011) Fundamentals of heat and mass transfer, 7th edn. Wiley, Hoboken
- Brundrett E, Baines WD (1964) The production and diffusion of vorticity in duct flow. *J Fluid Mech* 19:375–394
- Choi HS, Park TS (2013) The influence of streamwise vortices on turbulent heat transfer in rectangular ducts with various aspect ratios. *Int J Heat Fluid Flow* 40:1–14
- Fuchs T, Heinold M, Hain R, Kähler CJ (2014) Stereoscopic astigmatism particle tracking velocimetry for macroscopic 3D3C flow measurements in air. In: Proceedings of the 17th International symposium on applications of laser techniques to fluid mechanics lisbon, Portugal
- Gessner FB, Jones JB (1965) On some aspects of fully-developed turbulent flow in rectangular channels. *J Fluid Mech* 23:689–713
- Hussain AKMF, Reynolds WC (1975) Measurements in fully developed turbulent channel flow. *J Fluids Eng* 97:568–578
- Kwon YS, Philip J, de Silva CM, Hutchins N, Monty JP (2014) The quiescent core of turbulent channel flow. *J Fluid Mech* 751:228–254
- Lauder BE, Ying WM (1972) Secondary flows in ducts of square cross-section. *J Fluid Mech* 54:289–295
- Maas HG, Gruen A, Papantoniou D (1993) Particle tracking velocimetry in three-dimensional flows. *Exp Fluids* 15:133–147
- Melling A, Whitelaw JH (1976) Turbulent flow in a rectangular duct. *J Fluid Mech* 78:289–315
- Monty JP (2005) Developments in smooth wall turbulent duct flows, PhD thesis, The University of Melbourne
- Rochlitz H, Scholz P (2014) Wärmeübergangs-Versuche an einer generischen Kühlkanalgeometrie, vol 63. Deutscher Luft- und Raumfahrtkongress, Augsburg (DLR 2014-340014)
- Vázquez MS, Métais O (2002) Large-eddy simulation of the turbulent flow through a heated square duct. *J Fluid Mech* 453:201–238
- Vinuesa R, Noorani A, Lozano-Durán A, El Khoury GK, Schlatter P, Fischer PF, Nagib HM (2014) Aspect ratio effects in turbulent

- duct flows studied through direct numerical simulation. *J Turbul* 15(10):677–706
- Wardana ING, Ueda T, Mizomoto M (1992) Structure of turbulent two-dimensional channel flow with strongly heated wall. *Exp Fluids* 13(1):17–25
- Wardana ING, Ueda T, Mizomoto M (1994) Effect of strong wall heating on turbulence statistics of a channel flow. *Exp Fluids* 18(1–2):87–94
- Wieneke B (2005) Stereo-PIV using self-calibration on particle images. *Exp Fluids* 39:267–280